

## Co<sub>3</sub>O<sub>4</sub>/MnO<sub>2</sub> Core/Shell-Nanostructured Pseudocapacitor Electrode

Ji Hye Kwak,<sup>†</sup> Eun Joo Lee,<sup>†</sup> and Jin Ho Bang<sup>†,‡,\*</sup>

<sup>†</sup>Department of Bionanotechnology and <sup>‡</sup>Department of Chemistry and Applied Chemistry, Hanyang University, Kyeonggi-do 426-791, Korea. \*E-mail: jbang@hanyang.ac.kr

Received March 5, 2014, Accepted April 1, 2014

**Key Words** : Pseudocapacitor, Co<sub>3</sub>O<sub>4</sub>/MnO<sub>2</sub>, Capacitance, Synergic effect

Pseudocapacitors have received a great deal of attention as next-generation energy storage systems.<sup>1</sup> With high power density, specific capacitance, and the use of low-cost electrode materials, the pseudocapacitor has been considered an ideal system that is capable of bridging the gap between the electrical double-layer capacitor and the Li-ion battery. However, several issues, such as poor rate capability and cyclability resulting from the low electrical conductivity of the active materials, as well as Faradaic redox reactions for charge storage, must be addressed before practical utilization is feasible. A great deal of effort has been devoted to addressing these issues, including nanostructuring active materials, developing a novel electrode substrate, and synthesizing carbon-based nanocomposites.<sup>2-5</sup>

Among these strategies, utilizing multi-components for electrode materials has become popular due to the synergic effect from the use of multiple active materials. Various combinations such as Ni(OH)<sub>2</sub>/MnO<sub>2</sub>, Co<sub>3</sub>O<sub>4</sub>/MnO<sub>2</sub>, MoO<sub>2</sub>/Co(OH)<sub>2</sub>, and Co<sub>3</sub>O<sub>4</sub>/RuO<sub>2</sub> have been examined.<sup>6-9</sup> Among them, MnO<sub>2</sub>-based nanocomposites have received significant interest due to their abundance, high theoretical capacitance, and availability in a neutral electrolyte of MnO<sub>2</sub>.<sup>10</sup>

The combination of Co<sub>3</sub>O<sub>4</sub> and MnO<sub>2</sub> in particular is considered ideal, as Co<sub>3</sub>O<sub>4</sub> can serve as a conductive scaffold for MnO<sub>2</sub> due to its relatively good electrical conductivity, and can also improve the overall capacitance *via* its own redox reaction.<sup>7,11</sup> Fan *et al.* recently reported a Co<sub>3</sub>O<sub>4</sub>/MnO<sub>2</sub> core/shell array that exhibited high pseudocapacitive performance due to the synergic effect.<sup>7</sup> The synergistic contribution from both materials, however, was somewhat limited from the viewpoint of areal (C<sub>A</sub>) and gravimetric (C<sub>m</sub>) capacitances, which is a result of low mass loading. In general, achieving simultaneously high C<sub>A</sub> and C<sub>m</sub> poses a significant challenge, as increasing C<sub>A</sub> *via* a high mass loading of the active materials often leads to a dramatic decrease in C<sub>m</sub>, which originates from the large portion of dead material beneath electrode surface.<sup>12</sup> To address this issue, we designed a new nanoarchitecture, where core/shell-structured Co<sub>3</sub>O<sub>4</sub>/MnO<sub>2</sub> was conformally deposited on carbon fiber paper (CFP). CFP offers a porous structure, facilitating the access of electrolytes and alleviating the low electrical conductivity of electrode materials.<sup>13</sup> A thin Co<sub>3</sub>O<sub>4</sub> layer was conformally deposited over CFP *via* a one-step hydrothermal synthesis, and mesoporous MnO<sub>2</sub> nanoflakes were subsequently integrated over the Co<sub>3</sub>O<sub>4</sub> layer to further boost the charge storage

capability. By virtue of this rationally-designed electrode, the Co<sub>3</sub>O<sub>4</sub>/MnO<sub>2</sub> electrode on CFP showed good capacitive performance in terms of both areal and gravimetric capacitances, despite significant electrode material loading.

Co<sub>3</sub>O<sub>4</sub> is typically synthesized *via* a two-step process involving the synthesis of a Co<sub>3</sub>O<sub>4</sub> precursor such as Co(OH)<sub>2</sub>, followed by calcination for conversion to Co<sub>3</sub>O<sub>4</sub>. To avoid cumbersome post-annealing, Zhang *et al.* recently reported a new strategy for a single-step deposition of Co<sub>3</sub>O<sub>4</sub>.<sup>14</sup> In this approach, however, a substrate must be treated with HNO<sub>3</sub> prior to the reaction; otherwise only non-uniform Co(OH)<sub>2</sub> films would be obtained. However, unlike this report we found that CFP was capable of serving as a substrate for one-step hydrothermal deposition of Co<sub>3</sub>O<sub>4</sub> without any pre-treatment. This is advantageous because it not only shortened the reaction time, but also eliminated the need for a strong oxidant.

The formation of Co<sub>3</sub>O<sub>4</sub> was confirmed *via* X-ray diffraction (XRD) analysis (Figure 1(a)), where the intense diffraction peaks of Co<sub>3</sub>O<sub>4</sub> match those of standard Co<sub>3</sub>O<sub>4</sub> (JCPDS 42-1467). The average crystallite size from the (311) peak was 25.7 nm, determined using the Scherrer equation. Figure 1(b) shows the N<sub>2</sub> isotherm of Co<sub>3</sub>O<sub>4</sub>, where the type IV isotherm appeared with a type H4 hysteresis loop, which is

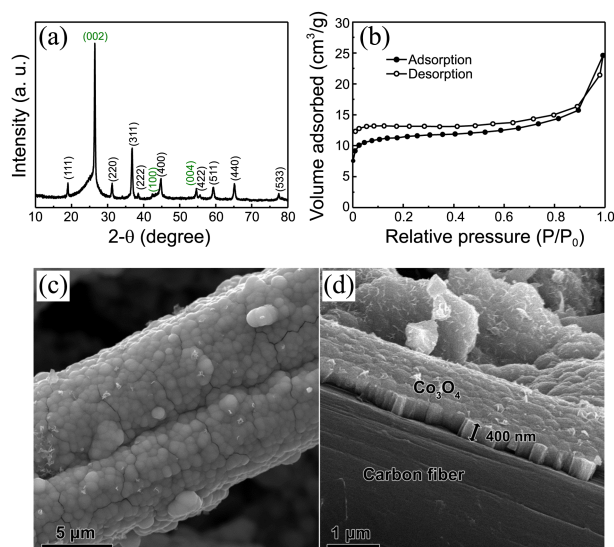


**Figure 1.** (a) XRD pattern (peaks from CFP are labeled in green), (b) nitrogen physisorption isotherm, and (c and d) SEM images of Co<sub>3</sub>O<sub>4</sub> deposited on CFP.

associated with narrow, slit-like pores.<sup>15</sup> The Brunauer-Emmett-Teller (BET) surface area was measured to be 43.3 m<sup>2</sup>/g. The morphology of the deposited Co<sub>3</sub>O<sub>4</sub> was examined *via* scanning electron microscopy (SEM), verifying the conformal deposit of a 400-nm-thick, uniform Co<sub>3</sub>O<sub>4</sub> film over the CFP (Figures 1(c) and 1(d)). Narrow, slit-like cracks were sporadically observed along the Co<sub>3</sub>O<sub>4</sub> film, which supported the type H4 hysteresis loop observed in the N<sub>2</sub> isotherm. Such conformal a coating with narrow slit-like pores could be beneficial for capacitive performance, as it could fully utilize the CFP surface and minimize dead Co<sub>3</sub>O<sub>4</sub> (not exposed to electrolyte), thus maximizing its utilization even with a significant amount of Co<sub>3</sub>O<sub>4</sub> loading. The growth of Co<sub>3</sub>O<sub>4</sub> was monitored *via* SEM analysis to elucidate the formation of conformal Co<sub>3</sub>O<sub>4</sub> film, as shown in Figure S1. During the initial reaction, no notable changes were observed within a 2 h period in the low-magnification SEM image. After 3 h, however, Co<sub>3</sub>O<sub>4</sub> nanoparticles were clearly visible, and more nanoparticles had formed and merged together, gradually filling the gap between the nanoparticles. Each carbon fiber was completely covered with the Co<sub>3</sub>O<sub>4</sub> nanoparticles after 8 h reaction time.

MnO<sub>2</sub> was subsequently deposited over the Co<sub>3</sub>O<sub>4</sub>/CFP electrode *via* a simple hydrothermal treatment for 30 min. In contrast to the commonly-performed, carbon-assisted reduction ( $4\text{MnO}_4^- + 3\text{C} + \text{H}_2\text{O} \rightarrow 4\text{MnO}_2 + \text{CO}_3^{2-} + 2\text{HCO}_3^-$ )<sup>16</sup> or electrodeposition,<sup>17</sup> our synthesis can quickly produce a thin, porous MnO<sub>2</sub> film without pre-carbon coating or destruction of the structural integrity of Co<sub>3</sub>O<sub>4</sub>. No noticeable change in pattern was observed in the initial XRD analysis when examining the crystal structure of MnO<sub>2</sub>. This may have been due to the intense diffraction peaks from Co<sub>3</sub>O<sub>4</sub> and CFP screening those from the thin MnO<sub>2</sub>. Raman spectroscopy was then carried out to characterize the MnO<sub>2</sub>, revealing the formation of  $\delta$ -MnO<sub>2</sub> (Figure 2(a)).<sup>18</sup> The formation of  $\delta$ -MnO<sub>2</sub> was also confirmed *via* the XRD

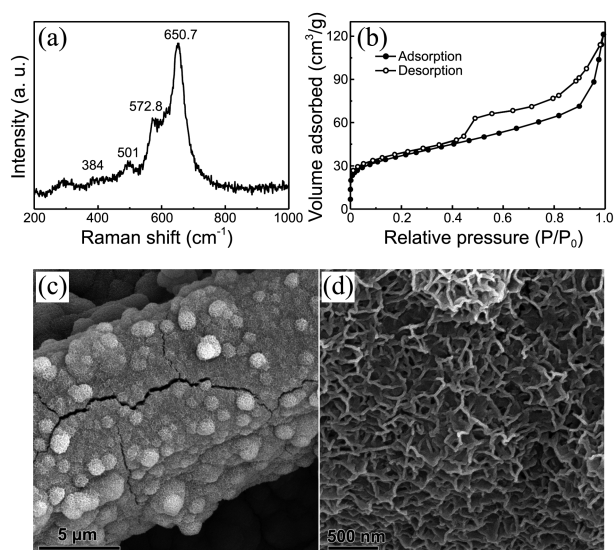


**Figure 2.** (a) Raman spectrum, (b) nitrogen physisorption isotherm, and (c and d) SEM images of the Co<sub>3</sub>O<sub>4</sub>/MnO<sub>2</sub> deposited on CFP.

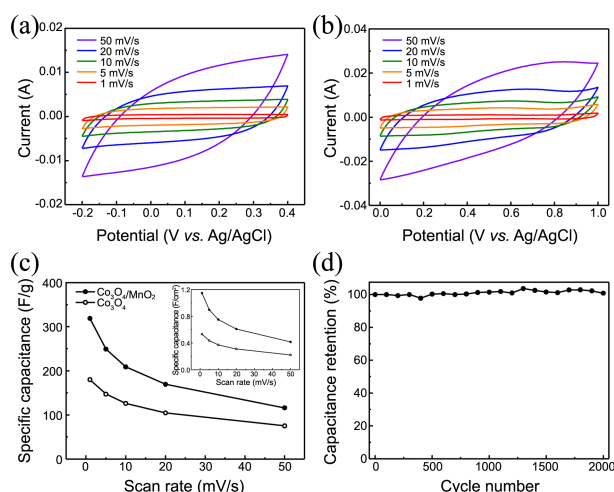


**Figure 3.** Cyclic voltammograms of (a) Co<sub>3</sub>O<sub>4</sub> and (b) Co<sub>3</sub>O<sub>4</sub>/MnO<sub>2</sub> electrodes at various scan rates, (c) gravimetric capacitance of Co<sub>3</sub>O<sub>4</sub> and Co<sub>3</sub>O<sub>4</sub>/MnO<sub>2</sub> electrodes at various scan rates (inset: areal capacitance), and (d) cycling performance of the Co<sub>3</sub>O<sub>4</sub>/MnO<sub>2</sub> electrode.

analysis of MnO<sub>2</sub> directly deposited on CFP (Figure S2). We determined from the type IV isotherm in the N<sub>2</sub> physisorption experiment (Figure 2(b)) that mesoporous MnO<sub>2</sub> was deposited, and its BET surface area was determined to be 130.2 m<sup>2</sup>/g. The SEM images in Figures 2(c) and 2(d) show that a myriad of thin MnO<sub>2</sub> nanoflakes were vertically integrated on the top of the Co<sub>3</sub>O<sub>4</sub>, with the morphology of Co<sub>3</sub>O<sub>4</sub> preserved. This porous structure could be advantageous for capacitive performance, because it promotes the accessibility of electrolytes to Co<sub>3</sub>O<sub>4</sub> covered in MnO<sub>2</sub>, and also creates more active sites for the redox reaction occurring on MnO<sub>2</sub>. Hence, the contribution from both active materials to the overall capacitance could be maximized.

Cyclic voltammetry (CV) measurement was conducted at various scan rates to investigate the electrochemical behavior of Co<sub>3</sub>O<sub>4</sub> and Co<sub>3</sub>O<sub>4</sub>/MnO<sub>2</sub> electrodes (Figures 3(a) and 3(b)). Both CV showed an ideal capacitive behavior with no distinctive redox peaks, signifying that they were charged and discharged at a pseudo-constant rate.<sup>19</sup> Figure 3(c) displays the C<sub>m</sub> and C<sub>A</sub> of Co<sub>3</sub>O<sub>4</sub> and Co<sub>3</sub>O<sub>4</sub>/MnO<sub>2</sub> electrodes at various scan rates. The Co<sub>3</sub>O<sub>4</sub>/MnO<sub>2</sub> electrode was superior to the Co<sub>3</sub>O<sub>4</sub> electrode in terms of C<sub>m</sub> and C<sub>A</sub> (319 F/g and 1.14 F/cm<sup>2</sup> at 1 mV/s), which was attributed to the synergistic effect of the two active materials. Even when compared with the MnO<sub>2</sub>/CFP electrode, the Co<sub>3</sub>O<sub>4</sub>/MnO<sub>2</sub> electrode exhibited a better performance, particularly at high scan rates (Figure S3). This indicates that the poor rate capability of the MnO<sub>2</sub>/CFP electrode was improved by depositing MnO<sub>2</sub> over the Co<sub>3</sub>O<sub>4</sub>. While the deposition of MnO<sub>2</sub> over Co<sub>3</sub>O<sub>4</sub> gave rise to an increase in electrical resistance, its capacitive loss was less than the benefit gained from the capacitive contribution of the Co<sub>3</sub>O<sub>4</sub>. The long-term stability of the Co<sub>3</sub>O<sub>4</sub>/MnO<sub>2</sub> electrode was examined *via* continuous potential sweeping at a scan rate of 100 mV/s (Figure 3(d)). No degradation in capacitance was observed, proving the excellent

stability of the  $\text{Co}_3\text{O}_4/\text{MnO}_2$  electrode.

In conclusions, a core/shell-structured  $\text{Co}_3\text{O}_4/\text{MnO}_2$  electrode on CFP was rationally designed to simultaneously achieve high  $C_m$  and  $C_A$ . A facile hydrothermal approach enabled the conformal deposition of a thin nanocomposite film on the CFP. The multiple-component electrode was superior to its single-component counterparts in terms of both  $C_m$  and  $C_A$ , a result of the synergic effect of the two active materials.

### Experimental

For  $\text{Co}_3\text{O}_4$  deposition, a piece of bare CFP (SGL Technologies, 1 cm × 5 cm) was soaked in a 100 mL, Teflon-lined, stainless steel autoclave that was filled with a solution containing cobalt nitrate hexahydrate (0.2 M) and 0.1 M ammonium nitrate dissolved in ammonium hydroxide solution (9 wt %). The autoclave was heated to 90 °C for 8 h, and was then naturally cooled. To deposit  $\text{MnO}_2$ , the black-colored CFP was thoroughly washed with deionized water, dipped again in the autoclave filled with an aqueous solution (40 mL) containing 71.2 mM  $\text{KMnO}_4$  and HCl (1 mL), and heated at 140 °C for 30 min. The amounts of  $\text{Co}_3\text{O}_4$  and  $\text{MnO}_2$  deposited on CFP were 2.0 and 2.3 mg/cm<sup>2</sup>, respectively.

$\text{Co}_3\text{O}_4$  and  $\text{MnO}_2$  were identified using an X-ray diffractometer (Rigaku D/Max-2500/PC) and a Renishaw 2000 confocal Raman microscope. The Brunauer–Emmett–Teller (BET) surface area was determined from the nitrogen adsorption/desorption isotherm measured using a BELSORP MINI II (BEL JAPAN). A scanning electron microscope (SEM, Hitachi S-4800 FESEM) was employed to examine the surface morphology of the electrodes. The electrochemical performance of the electrodes was investigated via a three-electrode system with an Ag/AgCl reference electrode and Pt counter electrode in 0.5 M  $\text{NaSO}_4$  electrolyte.  $C_A$  and  $C_m$  were determined via cyclic voltammetry (CV) performed at various scan rates using the following equation:  $C_A = \int I \cdot dt / (\Delta V \times S)$  and  $C_m = \int I \cdot dt / (\Delta V \times M)$ , where I is the oxidation/reduction current, dt is the time differential,  $\Delta V$  is the potential window, S is the geometrical area of the electrode, and M is the mass of the active material.

**Acknowledgments.** This work was supported by the research fund of Hanyang University (HY-2013-G).

**Supporting Information.** XRD pattern of  $\text{MnO}_2$  deposited on CFP; CVs and  $C_m$  and  $C_A$  of  $\text{MnO}_2$  electrode at different scan rates.

### References

1. Zhang, L. L.; Gu, Y.; Zhao, X. S. *J. Mater. Chem. A* **2013**, *1*, 9395-9408.
2. Jiang, J.; Li, Y.; Liu, J.; Huang, X.; Yuan, C.; Lou, X. W. *Adv. Mater.* **2012**, *24*, 5166-5180.
3. Cao, Y.; Yuan, F.; Yao, M.; Bang, J. H.; Lee, J.-H. *CrystEngComm* **2014**, *16*, 826-833.
4. Han, S.; Wu, D.; Li, S.; Zhang, F.; Feng, X. *Adv. Mater.* **2014**, *26*, 849-864.
5. Liu, J.; Lv, W.; Wei, W.; Zhang, C.; Li, Z.; Li, B.; Kang, F.; Yang, Q.-H. *J. Mater. Chem. A* **2014**, *2*, 3031-3037.
6. Jiang, H.; Li, C.; Sun, T.; Ma, J. *Chem. Commun.* **2012**, 2606-2608.
7. Liu, J.; Jiang, J.; Cheng, C.; Li, H.; Zhang, J.; Gong, H.; Fan, H. J. *Adv. Mater.* **2011**, *23*, 2076-2081.
8. Hercule, K. M.; Wei, Q.; Khan, A. M.; Zhao, Y.; Tian, X.; Mai, L. *Nano Lett.* **2013**, *13*, 5685-5691.
9. Xu, J.; Wang, Q.; Wang, X.; Xiang, Q.; Liang, B.; Chen, D.; Shen, G. *ACS Nano* **2013**, *7*, 5453-5462.
10. Gao, H.; Xiao, F.; Ching, C. B.; Duan, H. *ACS Appl. Mater. Interfaces* **2012**, *4*, 2801-2810.
11. Li, W.; Li, G.; Sun, J.; Zou, R.; Xu, K.; Sun, Y.; Chen, Z.; Yang, J.; Hu, J. *Nanoscale* **2013**, *5*, 2901-2908.
12. Kwak, J. H.; Lee, Y.-W.; Bang, J. H. *Mater. Lett.* **2013**, *110*, 237-240.
13. Lee, E. J.; Bang, J. H. *Mater. Lett.* **2013**, *105*, 28-31.
14. Yuan, C.; Yang, L.; Hou, L.; Shen, L.; Zhang, F.; Li, D.; Zhang, X. *J. Mater. Chem.* **2011**, *21*, 18183-18185.
15. Sing, K. S. W.; Everett, D. H.; Haul, R. A. W.; Moscou, L.; Pierotti, R. A.; Rouquerol, J.; Siemieniewska, T. *Pure Appl. Chem.* **1985**, *57*, 603-619.
16. Lei, Z.; Shi, F.; Lu, L. *ACS Appl. Mater. Interfaces* **2012**, *4*, 1058-1064.
17. Yang, P.; Li, Y.; Lin, Z.; Ding, Y.; Yue, S.; Wong, C. P.; Cai, X.; Tan, S.; Mai, W. *J. Mater. Chem. A* **2014**, *2*, 595-599.
18. Duay, J.; Sherrill, S. A.; Gui, Z.; Gillette, E.; Lee, S. B. *ACS Nano* **2013**, *7*, 1200-1214.
19. Yang, L.; Cheng, S.; Ding, Y.; Zhu, X.; Wang, Z. L.; Liu, M. *Nano Lett.* **2011**, *12*, 321-325.